

Kinetic Evaluation on Lithium Polysulfide in Weakly Solvating Electrolyte toward Practical Lithium–Sulfur Batteries

Xi-Yao Li, Shuai Feng, Yun-Wei Song, Chang-Xin Zhao, Zheng Li, Zi-Xian Chen, Qian Cheng, Xiang Chen, Xue-Qiang Zhang, Bo-Quan Li,* Jia-Qi Huang, and Qiang Zhang*



Cite This: *J. Am. Chem. Soc.* 2024, 146, 14754–14764



Read Online

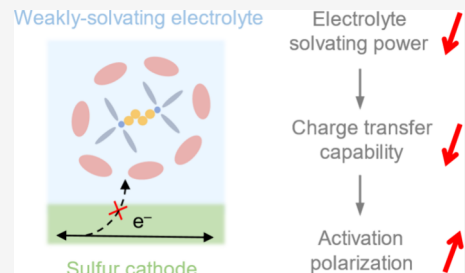
ACCESS |

Metrics & More

Article Recommendations

Supporting Information

ABSTRACT: Lithium–sulfur (Li–S) batteries are highly considered as next-generation energy storage techniques. Weakly solvating electrolyte with low lithium polysulfide (LiPS) solvating power promises Li anode protection and improved cycling stability. However, the cathodic LiPS kinetics is inevitably deteriorated, resulting in severe cathodic polarization and limited energy density. Herein, the LiPS kinetic degradation mechanism in weakly solvating electrolytes is disclosed to construct high-energy-density Li–S batteries. Activation polarization instead of concentration or ohmic polarization is identified as the dominant kinetic limitation, which originates from higher charge-transfer activation energy and a changed rate-determining step. To solve the kinetic issue, a titanium nitride (TiN) electrocatalyst is introduced and corresponding Li–S batteries exhibit reduced polarization, prolonged cycling lifespan, and high actual energy density of 381 Wh kg⁻¹ in 2.5 Ah-level pouch cells. This work clarifies the LiPS reaction mechanism in protective weakly solvating electrolytes and highlights the electrocatalytic regulation strategy toward high-energy-density and long-cycling Li–S batteries.



INTRODUCTION

The rapidly growing global energy consumption and the pursuit of a net carbon-zero society necessitate the development of renewable energy as well as high-efficient energy storage techniques.^{1,2} High-energy-density energy storage devices that exceed the current lithium-ion batteries are of great importance to multiple applications including portable electronics, electric vehicles, and smart grids.^{3–6} Lithium–sulfur (Li–S) batteries are promising candidates due to their ultrahigh theoretical energy density of 2600 Wh kg⁻¹ and environmental compatibility.^{7–9} Typical Li–S batteries are composed of carbon/sulfur composite cathodes, lithium metal anodes, and ether-based electrolyte.^{10–12} During the charge–discharge processes, the cathodic compartment undergoes complicated multiphase and multielectron redox reactions between solid elemental sulfur (S_8), soluble lithium polysulfides (LiPSs) in electrolyte, and solid lithium sulfide (Li_2S).^{13–16} Therein, LiPSs serve as key intermediates and their reactivity largely determines the Li–S battery performances.^{17–19} On one hand, the LiPSs dissolved in electrolyte break the kinetic limitation of direct solid–solid conversion between S_8 and Li_2S and accelerate the cathode reactions through an additional electrolyte-mediated pathway.^{20,21} On the other hand, the soluble LiPSs with high reactivity corrode lithium metal anodes and induce rapid anode failure.^{22,23} Additionally, the soluble LiPSs diffuse between the anodic and cathodic compartments and react on both the electrodes to render the notorious shuttle effect, reduced Coulombic efficiency (CE), and severe self-discharging in Li–S

batteries.^{24–26} As a result, the Li–S battery performances are highly dependent on the LiPS reactivity toward both the sulfur cathode and the lithium anode.^{27–30}

The LiPSs are solvated in electrolyte and their reactivity is largely determined by the solvating power of the electrolyte.^{31–33} In detail, the solvating power is ruled through the dipole–dipole interaction strength between the solvents and LiPSs in electrolyte, and it can be quantitatively reflected by the polarity (dielectric constant ϵ) and donicity (Gutmann donor number DN).^{34,35} Generally, electrolytes with strong solvating power (denoted as strongly solvating electrolytes) composed of high polarity or donicity solvents interact with LiPSs tightly and endow LiPSs with high reactivity.^{36,37} However, the drastic parasitic reactions between LiPSs and Li anodes in strongly solvating electrolytes always render rapid anode failure and cannot even maintain the basic operation of practical Li–S batteries with limited Li excess.^{38,39} In converse, electrolytes with weak solvating power (denoted as weakly solvating electrolytes) constituted by low polarity or donicity solvents have weak interactions with LiPSs; thus, the LiPS reactivity therein is relatively lessened.^{40,41} As a result, the low LiPS reactivity in weakly solvating electrolytes promises Li

Received: February 21, 2024

Revised: May 3, 2024

Accepted: May 6, 2024

Published: May 16, 2024



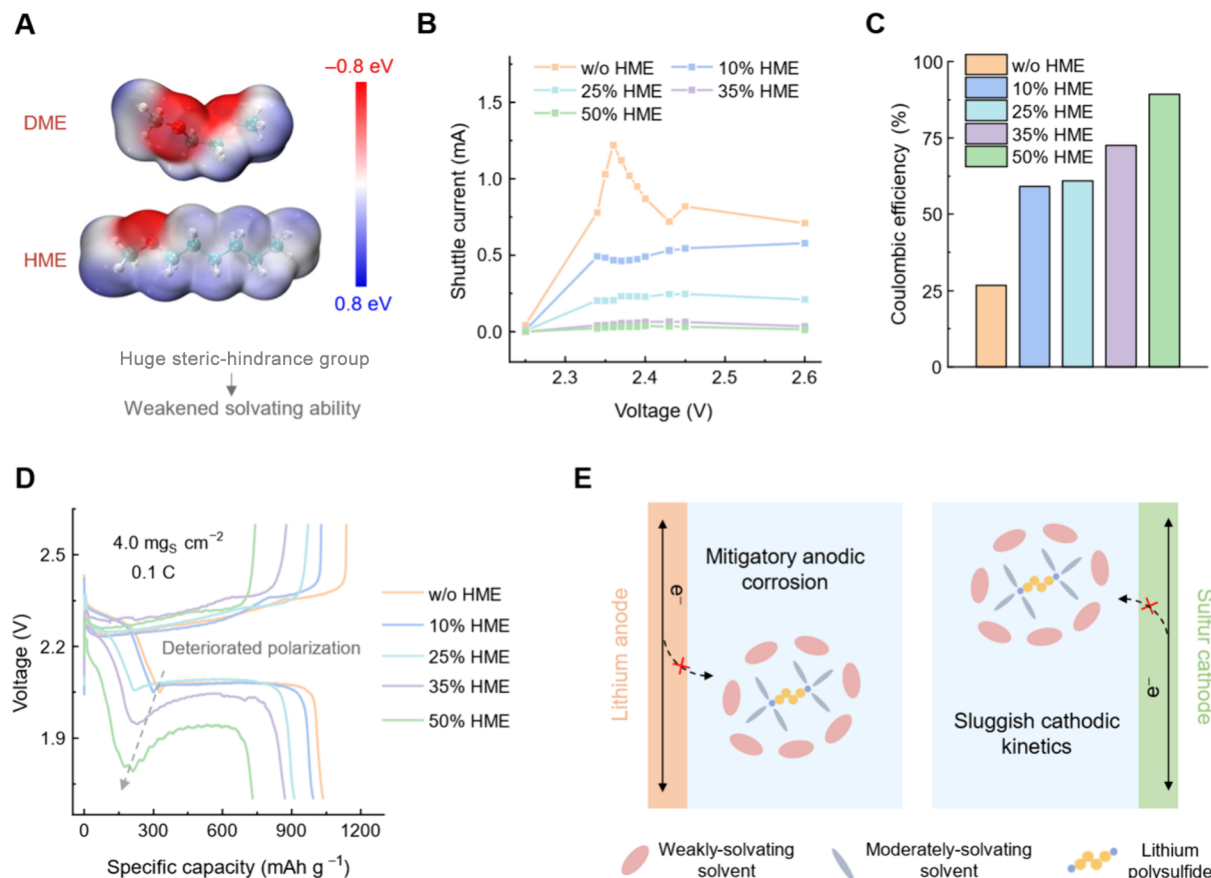


Figure 1. Construction and evaluation of weakly solvating electrolyte on lithium anodes and sulfur cathodes. (A) Electrostatic potentials of the moderately solvating solvent (DME) and weakly solvating solvent (HME) (isovalue: 0.001 a.u.). The hydrogen, carbon, and oxygen atoms are marked with white, gray, and red, respectively. (B) Shuttle currents at various potentiostatic charging voltages. (C) CE evaluation in Li–S coin cells. (D) Charge–discharge profiles in Li–S coin cells under harsh conditions. (E) Schematic of the LiPS anodic and cathodic behaviors in weakly solvating electrolyte.

anode protection and improved cycling stability even in practical Li–S batteries with limited Li excess.^{42–44} For instance, Hou et al. adopted a di-isopropyl sulfide (DIPS) solvent with low polarity and donicity to construct weakly solvating electrolytes, which effectively lowered the LiPS reactivity and endowed Ah-level Li–S pouch cells with a lifespan over 100 cycles.⁴⁵ The above remarkable performances of Li–S batteries evidently manifest the potential of employing promising weakly solvating electrolytes.⁴⁶ However, although the weakly solvating electrolytes improve the cycling stability, they also degrade LiPS kinetics in cathode reactions, thereby increasing polarization, reducing discharge capacity, and lowering energy density especially in practical pouch cells.^{47–50} The kinetic degradation mechanism in protective weakly solvating electrolytes is quite unclear, and targeted strategies toward practical high-energy-density Li–S batteries with weakly solvating electrolytes are rarely proposed.

In this contribution, the cathodic LiPS kinetic degradation mechanism in weakly solvating electrolytes is disclosed to construct high-energy-density Li–S batteries. The weakly solvating electrolyte is constructed by using hexyl methyl ether (HME) as an exemplificative weakly solvating solvent, where electrolytes with higher HME content exhibit weaker solvating power for LiPSs. The polarization decoupling results identify the dramatically increased activation polarization, instead of concentration or ohmic polarization, as the dominant kinetic limitation when the LiPS solvating power

of the electrolyte decreases. Further mechanism investigation indicates the enlarged activation polarization originates from higher activation energy of the charge transfer process and a changed rate-determining step. To address the above kinetic issue, titanium nitride (TiN) is introduced as an effective LiPS electrocatalyst to overcome unbearable activation polarization. Consequently, Li–S batteries with HME-based weakly solvating electrolyte and a TiN electrocatalyst exhibit reduced polarization, ultrahigh specific capacity over 1200 mAh g⁻¹, and prolonged cycling lifespan for nearly 100 cycles in Li–S cells using 4.0 mg_S cm⁻²-loading sulfur cathodes and 50 μm-thick lithium anodes. Furthermore, the practical application potential of the weakly solvating electrolytes is demonstrated in 2.5 Ah-level Li–S pouch cells with an actual energy density of 381 Wh kg⁻¹.

RESULTS AND DISCUSSION

To construct the weakly solvating electrolytes, a weakly solvating HME solvent and conventional 1,3-dioxolane (DOL)/1,2-dimethoxyethane (DME) solvents were mixed with variable ratios, where the HME solvent is compatible with DOL/DME mixed solvents in solubility without phase separation. From the molecular level, the solvating power of HME, DOL, and DME is highly related to their molecular structures. Generally, it is deemed that the oxygen atom with lone-pair electrons in the solvent molecules serves as the coordinating site for LiPS solvation.⁵¹ In the HME molecule, a

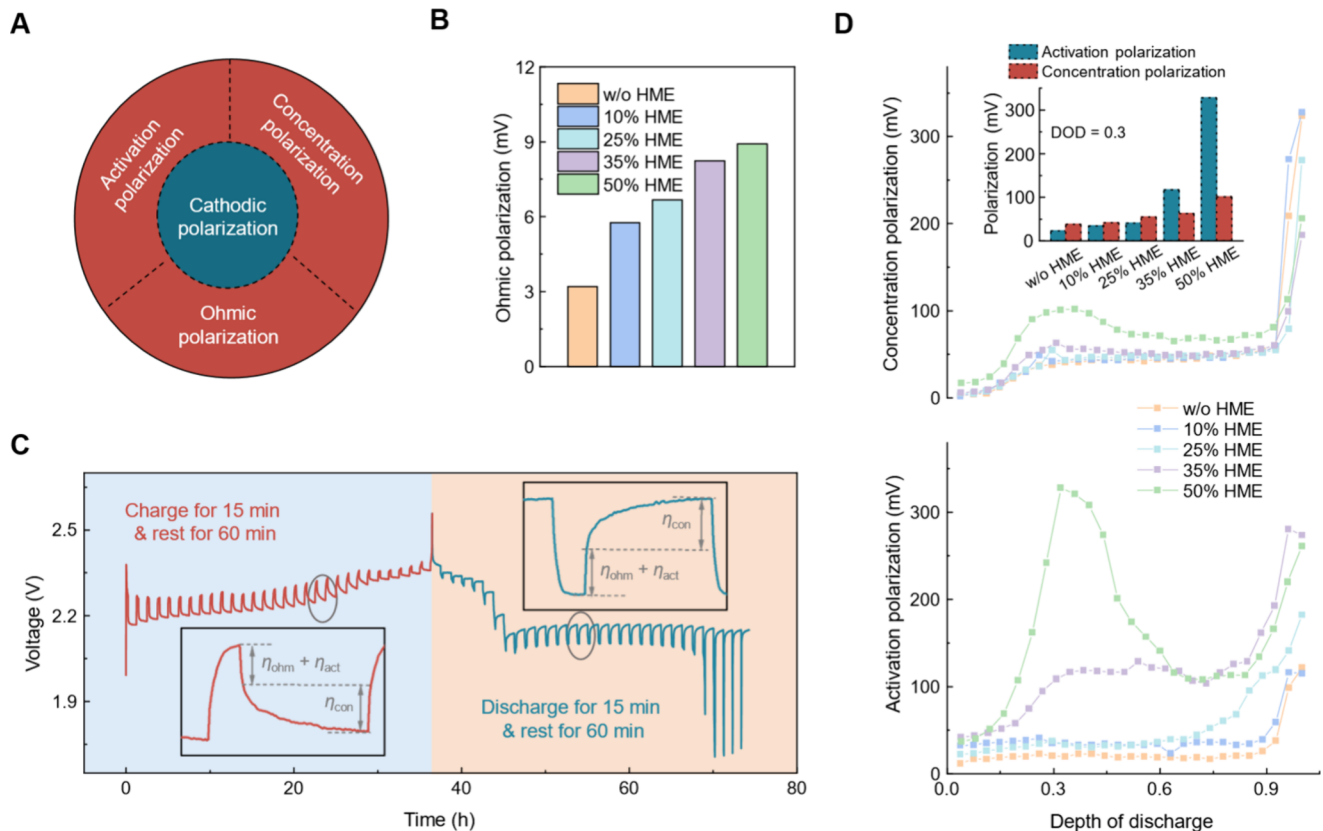


Figure 2. Decoupling of the cathodic polarizations in Li–S full cells with weakly solvating electrolytes. (A) Schematic of the cathodic polarizations. (B) Ohmic polarizations measured by EIS techniques. (C) Schematic of polarization decoupling by GITT methods, where detailed processing procedures are magnified in the inset figure. (D) Concentration polarizations (the upper figure) and activation polarizations (the bottom figure) versus the depth of discharge (DOD) and their comparison at DOD = 0.3 (the inset figure).

huge steric-hindrance *n*-hexyl group ($n\text{-C}_6\text{H}_{13}-$) is adjacent to the oxygen atom, which makes it difficult for the lone-pair electron in the oxygen $2p$ orbitals to be donated to the Li $2s$ empty orbital in LiPS molecules (Figure S1). Namely, the HME solvent exhibits weak LiPS solvating power due to the large steric-hindrance group. The electrostatic potential calculations further manifest the weak solvating power of HME. In detail, the negative charges are confined near the oxygen atom region in the HME molecule compared with DOL and DME, illustrating less possibility for HME to interact with the positive charges in LiPSs (Figure 1A). Furthermore, the negative Mulliken charge on the oxygen atom in HME ($0.23\text{ }e^-$) is much reduced compared with those in DOL and DME (0.49 and $0.52\text{ }e^-$, respectively), illustrating the much weaker LiPS solvating power of HME than DOL and DME (Figure S2). In this way, when increasing the HME content in the electrolyte, the solvating power of the electrolyte will be accordingly weakened in principle. The experimental results of the electrolyte donicity also prove the above results. Electrolytes with variable HME contents from 0% to 50% were prepared after dissolving lithium salts (denoted as HME solutions), and their donor numbers were quantified by nuclear magnetic resonance (NMR) spectroscopy (Figure S3). The donor number of the HME solutions decreases from 16.6 to 15.5 kcal mol⁻¹ when the HME content increases from 0% to 50%, evidently manifesting that the electrolyte solvating power is accordingly weakened as the HME content increases. The Li_2S_8 and Li_2S_6 solubilities also decrease along with the increment of the HME content in electrolyte, where the Li_2S_8

solvability reduces from 4.2 to 1.3 mol_[S] L⁻¹ and the Li_2S_6 solvability reduces from 3.3 to 1.2 mol_[S] L⁻¹ when the HME content increases from 0 to 50% (Figure S4). Considering the decreased donor number and reduced LiPS solubility, the electrolyte solvating power is weakened as the HME content increases.

To correlate the reactivity between LiPS and Li metal anode with the electrolytes' solvating power, shuttle currents were tested in cells with the HME solutions (Figure 1B). The shuttle currents successively decrease along with the increment of the HME content (e.g., 1.22, 0.47, 0.21, 0.05, and 0.03 mA at 2.36 V for 0%, 10%, 25%, 35%, and 50% HME solutions, respectively), indicating that the anodic parasitic reactions are better inhibited in a high-HME-content electrolyte. The CE evaluations in Li–S coin cells also manifest the restrained LiPS anodic reactivity in high-HME-content electrolytes (Figure S5). Concretely, the CE value is promoted from 26.7% to 89.3% in model tests when the HME content changes from 0% to 50%, illustrating that the LiPS anodic parasitic reactions and corosions are reduced as the HME content increases (Figure 1C). The CE value in Li–S batteries with LiNO_3 additives is also promoted when the HME content increases (Figure S6). In brief, the LiPS anodic reactivity is reduced as the electrolyte solvating power gets weakened.

Investigations of the LiPS cathodic reactivity are further conducted in cells adopting HME electrolytes with LiNO_3 additives using $4.0\text{ mg}_\text{S}\text{ cm}^{-2}$ -loading sulfur cathodes. Under a small rate of 0.05 C ($1\text{ C} = 1672\text{ mA g}_\text{S}^{-1}$), the Li–S cells exhibit analogous polarizations and comparable specific

capacities in every HME electrolyte, illustrating the cathodic kinetics of LiPSs are not severely affected under mild conditions (Figure S7). However, both the polarizations and the specific capacities are badly aggravated under a larger rate of 0.1 C, and such phenomena in the discharge process are especially notable (Figure 1D). In detail, a huge dip emerges between the two discharge plateaus in the Li–S cells with 35% or 50% HME electrolytes, and the minimum voltages in the above dips reach 1.95 and 1.79 V, respectively. The unbearably increasing polarizations prove that the apparent kinetics for LiPSs becomes more sluggish along with the decrease of the electrolyte solvating power under harsh working conditions.

Combining the LiPS anodic and cathodic reactivity evaluations, we can get preliminary conclusions that with the decrease of the electrolyte solvating power, the LiPS anodic corosions are greatly mitigated, but the LiPS cathodic kinetics are severely deteriorated (Figure 1E). Since the deteriorated cathodic LiPS kinetics result in inferior battery performances, it is essential to clarify the cathodic kinetic degradation mechanism and the underlying chemistry therein in weakly solvating electrolytes.

To disclose the cathodic kinetic degradation mechanism in weakly solvating electrolytes, the cathodic polarization is selected as the key indicator to reflect the dominant kinetic limitation as the LiPS solvating power of the electrolyte decreases. In detail, the cathodic polarization can be decoupled into ohmic, concentration, and activation polarizations (Figure 2A). The ohmic polarization (η_{ohm}) originates from ionic and electronic resistance in bulk electrodes and electrolytes, the concentration polarization (η_{con}) is ascribed to the sluggish mass transfer (mainly diffusion) of the active species from the bulk electrolyte to the electrode surface, and the activation polarization (η_{act}) originates from the sluggish charge transfer kinetics of the interfacial redox reactions. Each of the above three polarizations may be the dominant cause for the enlarged overall polarizations with higher HME content; thus, quantifying their proportions is rather significant.

To quantify the proportions of the above three polarizations in Li–S batteries, electrochemical impedance spectroscopy (EIS) analysis and the galvanostatic intermittent titration technique (GITT) are combined. In detail, the internal bulk resistance (R_{bulk}) is simulated according to the EIS Nyquist plots, and its value after being multiplied by the testing current (I) is regarded as η_{ohm} according to the Ohm's Law (Figure S8). Experimentally, the values of η_{ohm} increase from 3.20, 5.76, 6.67, and 8.24 to 8.92 mV as the HME content changes from 0%, 10%, 25%, and 35% to 50% (Figure 2B). The enlarged η_{ohm} is due to the lowered electrolyte ionic conductivity with higher HME content (Figures S9 and S10). The η_{act} and η_{con} values are distinguished from the voltage–time profiles in the GITT tests (Figure 2C). Concretely, the Li–S cells were charged or discharged at 0.1 C for 15 min to make the kinetics issues and respective polarizations exposed. Afterward, the Li–S cells were rested for 60 min to make the polarizations eliminated; thus, the cells reach the thermodynamic equilibrium states. Taking the discharge process in one step as an example (Figure 2C, inset figure), the voltage declines during the discharge process and rises during the rest of the process. Notably, η_{act} and η_{ohm} are directly relevant to the applied current according to the Butler–Volmer equation and Ohm's Law, respectively. Therefore, η_{act} and η_{ohm} will be immediately eliminated when the applied current is repealed. On the contrary, the mass transfer

process is time-dependent according to the Nernst–Planck equation. Accordingly, η_{con} will be gradually eliminated along time relaxation after the applied current is repealed. Therefore, during the rest of the process, the voltage rises sharply at the beginning corresponding to the elimination of η_{act} and η_{ohm} while it rises gradually in the subsequent relaxation process corresponding to the elimination of η_{con} . Based on the above analysis, the proportions of each polarization can be accurately quantified (Figure 2D and Figure S11).

Since the kinetic issues in the discharge process are much more severe than those in the charge process (the maximum polarization value during the discharge process is twice higher than that during the charge process as shown in Figure S12), the polarization distribution analysis for the discharge process is emphasized. Therein, the polarization variations along with the alteration of both depth of discharge (DOD) and HME content should be paid attention to.

In detail, for each electrolyte, with the increment of DOD, the value of η_{ohm} takes up a tiny proportion throughout the discharge process (around 5%), manifesting electron or ion conductivity is not the main cause for the sluggish kinetics (Figure S13). For η_{act} and η_{con} taking up the dominant proportion, the $\eta_{\text{act}}\text{--DOD}$ and $\eta_{\text{con}}\text{--DOD}$ curves exhibit a peak shape, and the maximum value emerges around DOD = 0.3 (Figure S14). Notably, the DOD = 0.3 approximately corresponds to the state of maximum LiPS concentration and the initiation of Li_2S deposition from LiPSs. Comparing the polarizations at DOD = 0.3 in the electrolytes with variable HME contents, the value of η_{con} increases from 38.0 to 101 mV as the HME content rises from 0% to 50%, which can be explained by the hindered diffusion procedure with higher HME content (Figures S15–S17). Meanwhile, the value of η_{act} increases more rapidly from 22.7, 34.3, 41.2, and 117 to 328 mV as the HME content rises from 0%, 10%, 25%, and 35% to 50% at DOD = 0.3. Worthy to be noted, the value of η_{act} is much higher than η_{con} in the cells with 35% and 50% HME electrolytes (1.86 and 3.25 times at DOD = 0.3, respectively, Figure 2D, inset). The more rapidly enlarged η_{act} than η_{con} suggests that the intrinsic LiPS interfacial charge transfer kinetics is more severely deteriorated than the LiPS diffusion capability with a higher HME content in the electrolyte. To examine the universality of the LiPS degradation mechanism in a weakly solvating electrolyte, another typical weakly solvating solvent with huge steric hindrance, 1,1,2,2-tetrafluoroethyl-2,2,3,3-tetrafluoropropyl ether (TTE), is introduced to construct a weakly solvating electrolyte for Li–S batteries (Figures S18–S20). The polarization decoupling analysis illustrates that the η_{act} is still the dominant kinetics limitation, which is consistent with the conclusions drawn in the HME electrolytes. In brief, the above results evidently illustrate that the unbearably increased η_{act} instead of η_{ohm} or η_{con} should be blamed for the sluggish kinetics with the reduction of the electrolyte solvating power.

As discussed above, the rapidly enlarged η_{act} accounts for the main cause of the unbearable polarizations in weakly solvating electrolytes, while the underlying chemistry therein is still unclear. Notably, the high η_{act} particularly exists at DOD = 0.3 corresponding to the end of the liquid–liquid conversion process between the dissolved LiPSs and the beginning of the liquid–solid conversion process regarding solid Li_2S nucleation and deposition. Therefore, investigations of the intrinsic kinetics in both liquid–liquid and liquid–solid conversion processes are conducted.

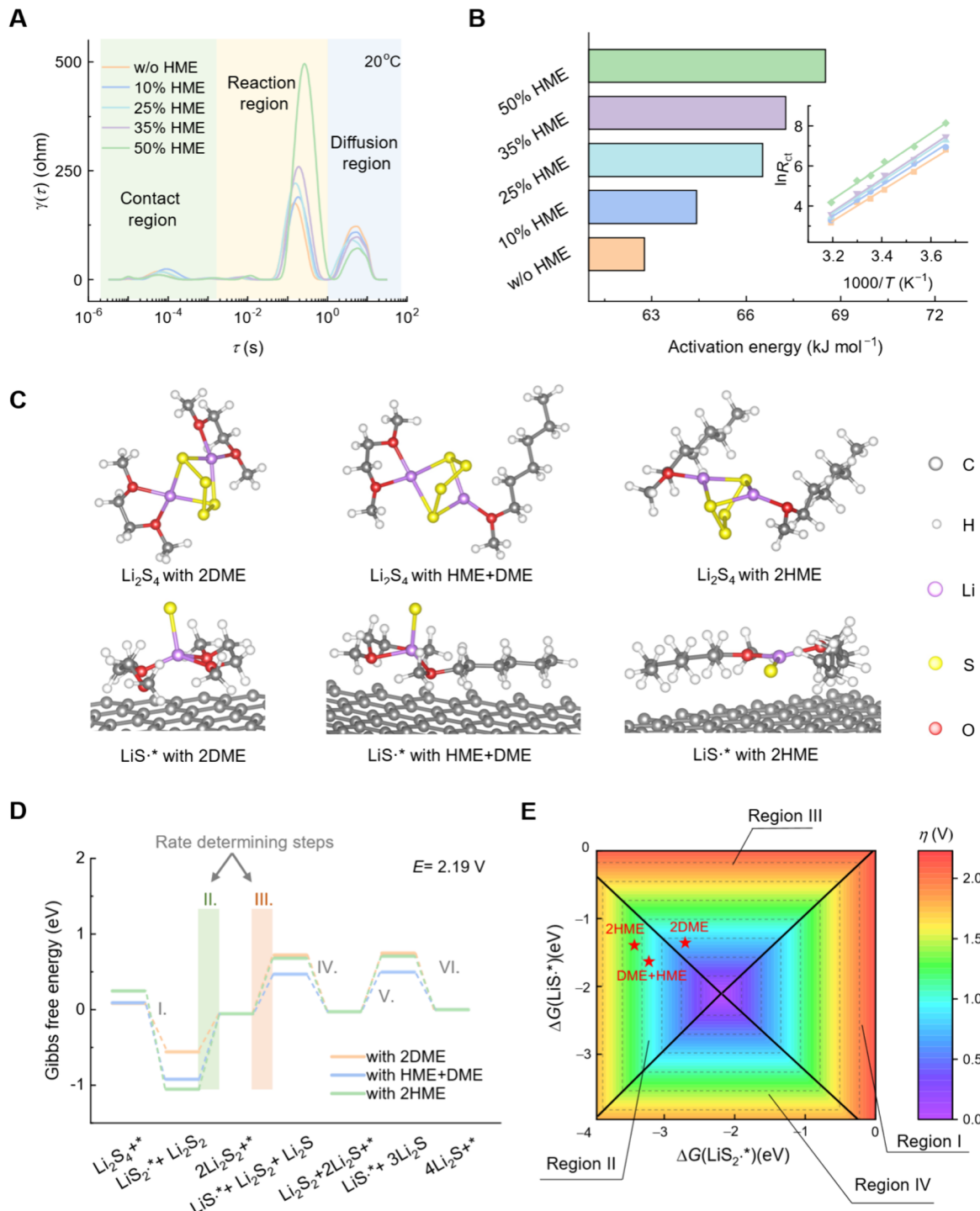


Figure 3. Intrinsic LiPS cathodic kinetics evaluation in weakly solvating electrolytes regarding (A, B) liquid–liquid and (C–E) liquid–solid conversions. (A) DRT analysis of Li_2S_6 symmetric cells at 20 °C. (B) Activation energies for the charge transfer process and their fitting procedure through the Arrhenius equation (the inset figure). (C) Optimized structures of Li_2S_4 (the upper figures) and LiS^* (the bottom figures) interacting with solvents, where * represents the graphene substrate. (D) Calculated Gibbs free energy diagrams of the liquid–solid conversion from Li_2S_4 to Li_2S at the equilibrium potential in 2DME, DME+HME, and 2HME electrolytes. (E) Regional diagrams of overpotential versus $\Delta G(\text{LiS}^*)$ and $\Delta G(\text{LiS}_2^*)$ corresponding to the liquid–solid conversion from Li_2S_4 to Li_2S .

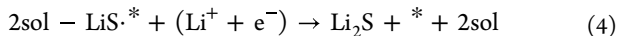
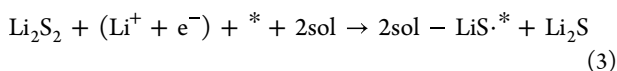
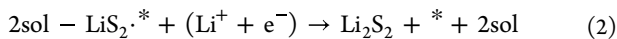
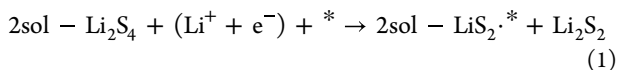
For the liquid–liquid conversions, the interfacial electrochemical reactions involve two steps: reactant adsorption and charge transfer. To probe the adsorption behavior of LiPSs in weakly solvating electrolytes, in situ ultraviolet–visible (UV–vis) spectroscopy analyses were conducted. Concretely, Li_2S_8 serving as the model reactant was dissolved in electrolyte with different HME contents, and graphene serving as the model

electrode matrix was immersed in the electrolytes (Figure S21, detailed experimental procedure in section 1.5 of the Supporting Information). According to the UV–vis spectroscopy results, the equilibrium adsorption capacities (Q_{\max}) are around $2.7 \times 10^{-3} \text{ mmol}_{[\text{Li}_2\text{S}_8]} \text{ mg}_G^{-1}$ and the adsorption rate constants (k_{ads}) are around 0.09 h^{-1} in the different HME-content electrolytes. The almost the same Q_{\max} and k_{ads} values

illustrate that the Li_2S_8 adsorption upper limit and adsorption rates are not changed in weakly solvating electrolytes (Figures S22 and S23). Therefore, the rate-limiting step of the liquid–liquid conversions in weakly solvating electrolytes is not the adsorption process as the electrolyte solvating power decreases.

To probe the charge transfer process in liquid–liquid conversions, EIS tests and distribution relaxation time (DRT) analyses on Li_2S_6 symmetric cells were applied (Figure S24). According to the DRT spectroscopy, three distinct peaks emerge around the characteristic relaxation time (τ) of 10^{-4} , 10^{-1} , and 10^1 s, corresponding to the contact region, the reaction region, and the diffusion region, respectively (Figure 3A). Additionally, the above characteristic processes with specific physical meanings can be depicted by the parallel of resistance (R) and capacitance (C) in the equivalent circuit model (Figure S25). Therein, the charge transfer resistance (R_{ct}) is an important indicator of the energy barrier in the charge transfer step. In detail, Li_2S_6 symmetric cells with variable HME-content electrolytes were tested under different temperatures (T) from 0 to 40 °C, where the value of R_{ct} rises along with reduced temperatures (Figure S26). Fitted by the Arrhenius equation, the activated energy increases from 62.8 to 68.5 kJ mol⁻¹ when the HME content in the electrolyte rises from 0% to 50% (Figure 3B). As a result, the enlarged activated energy directly induces the aggravation of the charge transfer kinetics and further hampers the liquid–liquid conversion kinetics in Li–S batteries as the electrolyte solvating power gets weakened.

To probe the intrinsic kinetics in LiPS liquid–solid conversions, density functional theory (DFT) calculations were conducted on the conversion from Li_2S_4 to Li_2S . The solvation effect is considered by introducing extra solvents. Specifically, 2DME, DME+HME, or 2HME molecules were added to both reactants and intermediates, i.e., solvated Li_2S_4 molecules and LiPS radicals on the substrate (Figure 3C, Figure S27 and S28). Based on our previous study on the mechanism of the sulfur reduction reaction, the preferential pathway is the Li_2S_4 symmetrical decomposition, where Li_2S_4 molecules convert to Li_2S_2 first and then to Li_2S finally.⁵² The detailed hypothesized elementary reactions are as follows:



Therein, * represents graphene as the reaction substrate, and 2sol represents two solvent molecules (2DME, DME+HME, or 2HME). Li_2S_2 and Li_2S are regarded as crystals (Figures S29 and S30). Based on the above four elementary reactions 1–4, the six-electron-transfer process from Li_2S_4 to Li_2S can be divided into six single-electron-transfer steps (Figure 3D, detailed Step I–VI in section 1.11.2 of Supporting Information). The Gibbs-free-energy evolution of Step I–VI is accurately computed at the potential of 0 V (vs Li/Li⁺) (Figure S31 and Table S1) and further depicted at the equilibrium potential ($E_{eq} = 2.19$ V) through the *ab initio* simulations (Table S2). From the Gibbs-free-energy evolution diagrams at E_{eq} , the calculated overpotential for LiPSs solvated

by 2DME, HME+DME, or 2HME is 0.78, 0.87, and 1.00 V, respectively (Figure S32). The incremental calculated overpotentials evidently manifest the aggravated intrinsic electrochemical redox kinetic sluggishness for the liquid–solid conversion process in weakly solvating electrolytes.

Moreover, the rate-determining step (i.e., the step with the largest energy barrier) is altered from Step III into Step II as the HME content rises (Figure 3D). Concretely, two energy barriers are exhibited in Step II and Step III for all three systems with 2DME, HME+DME, or 2HME, illustrating that both the decomposition of $2\text{sol}-\text{LiS}_2\cdot^*$ and the generation of $2\text{sol}-\text{LiS}\cdot^*$ are kinetically unfavored in LiPS liquid–solid conversions. Notably, the largest energy barrier emerges in Step III for the system with 2DME while it lies in Step II for the systems with HME+DME or 2HME (Table S2). To quantify the above observation, two descriptors, $\Delta G(\text{LiS}_2\cdot^*)$ and $\Delta G(\text{LiS}\cdot^*)$, are introduced and defined as the Gibbs free energy changes of reactions 1 and 3 (detailed discussion in section 1.11.3 of the Supporting Information). Based on these two descriptors, reactions 1–4 can be quantitatively depicted as four regions in three-dimensional volcano plots, where the system with 2DME locates in Region III ($\Delta G(\text{LiS}_2\cdot^*) = -1.30$ eV, $\Delta G(\text{LiS}\cdot^*) = -2.65$ eV), but the systems with HME+DME ($\Delta G(\text{LiS}_2\cdot^*) = -0.77$ eV, $\Delta G(\text{LiS}\cdot^*) = -2.40$ eV) and 2HME ($\Delta G(\text{LiS}_2\cdot^*) = -0.58$ eV, $\Delta G(\text{LiS}\cdot^*) = -2.60$ eV) locate in Region II (Figure 3E). The above phenomena demonstrate that the $\text{LiS}_2\cdot$ radical solvated by HME is more difficult to gain an electron and be converted to Li_2S_2 compared with that solvated by DME, which hinders the overall LiPS redox kinetics and induces enlarged overpotential of the liquid–solid conversion processes in weakly solvating electrolyte (Figure S33). Furthermore, the binding energies of the LiPS radicals on graphene substrate are greatly enlarged as the electrolyte solvating power gets weakened (e.g., 0.82, 1.27, and 1.50 eV for $\text{LiS}_2\cdot$ solvated by 2DME, DME+HME, or 2HME, respectively), which makes it harder to be desorbed from the substrate and hinders the following reactions (Figure S34). In brief, due to the altered rate-determining step and accordingly larger energy barriers in the elemental reactions, the intrinsic liquid–solid conversion kinetics is impaired in weakly solvating electrolytes. Combining the evaluation results for liquid–liquid and liquid–solid conversions together, it can be concluded that the hampered charge transfer process reduces the intrinsic LiPS reactivity, impedes the LiPS redox kinetics, and triggers the enlarged η_{act} in weakly solvating electrolytes.

To examine the effects of weakly solvating electrolyte at the cell level, LiLi_2S_6 cells were assembled adopting Li_2S_6 electrolytes with variable HME contents and evaluated via cyclic voltammetry (CV) tests (Figure S35). Two reduction peaks (R_1 and R_2 regarding the Li_2S precipitation and the S_8 dissolution, respectively) and two oxidation peaks (O_1 and O_2 regarding the Li_2S oxidation and the S_8 precipitation, respectively) explicitly emerge in each cell with the different HME electrolytes in the CV profiles, illustrating that the basic conversion types of the sulfur species are not altered as the electrolyte solvating power is weakened. Generally, the sulfur redox kinetics can be reflected by the onset potential as quantitative evaluation indicators since the LiPS diffusion process forced by concentration gradients merely exist at this stage. In detail, the onset potential for process O_1 increases from 2.19 to 2.24 V when the HME content rises from 0% to 50%, and the enlarged oxidation overpotential manifests that the Li_2S oxidation redox kinetics gets sluggish as the electrolyte

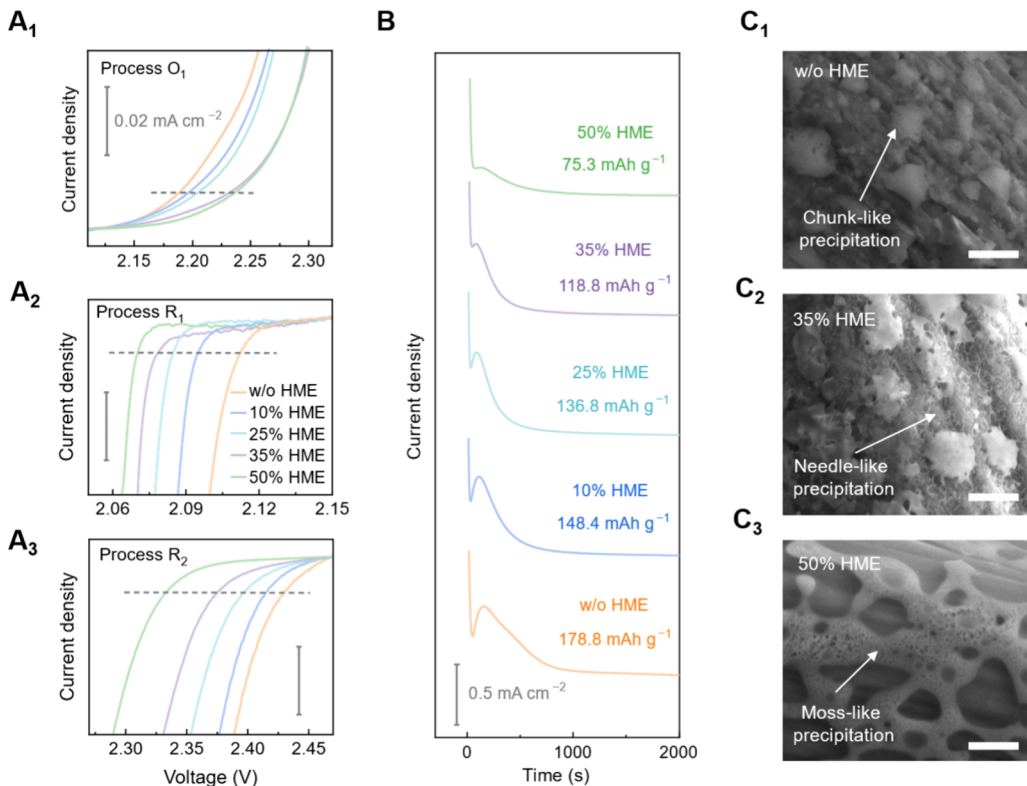


Figure 4. Apparent LiPS kinetics evaluation in weakly solvating electrolytes. Magnified CV profiles of the LiLi₂S₆ cells involving (A₁) the Li₂S oxidation, (A₂) the Li₂S precipitation, and (A₃) the S₈ dissolution processes. The gray dashed lines in (A₁–A₃) mark the onset potentials (versus Li⁺/Li). (B) Potentiostatic discharge profiles of the Li|CP cells with Li₂S₆ dissolving in HME solutions. (C₁–C₃) High-resolution SEM images of the Li₂S precipitates on CP electrodes (scale bar: 1 μm).

solvating power gets weakened (Figure 4A₁). In addition, the R₁ and R₂ processes exhibit analogous tendencies in that the onset potential decreases from 2.11 to 2.07 V for process R₁ and from 2.43 to 2.33 V for process R₂ (Figure 4A₂–A₃). Conclusively, the weakly solvating-electrolyte effect on hampering the LiPS redox kinetics is of full range including the LiPS oxidation and reduction processes.

Since the Li₂S precipitation process (process R₁) dominates the capacity in the discharge process, it is essential to specially investigate the effects of the weakly solvating electrolytes on the Li₂S precipitation process. Concretely, potentiostatic tests were adopted on Li|CP cells to evaluate the process of dissolved LiPSs converting to solid Li₂S (Figure 4B). The precipitation capacity integrated in the potentiostatic profile decreases from 178.8 to 75.3 mAh g⁻¹ when the HME content increases from 0% to 50%, illustrating the Li₂S precipitation extent is badly impaired in weakly solvating electrolytes. Additionally, according to the energy-dispersive X-ray spectra (EDS) analysis, the sulfur content of the CP electrode after Li₂S precipitation decreases from 17.1% to 3.1% as the HME content increases (Figure S36), the tendency of which is in accordance with the Li₂S precipitation capacity results. Furthermore, the Li₂S precipitation morphologies on the CP electrodes were investigated, where three types of Li₂S morphologies are observed in the scanning electron microscopy (SEM) images (Figure S37). Concretely, the Li₂S morphology changes from chunk-like (Figure 4C₁) to needle-like (Figure 4C₂) and finally converts to moss-like precipitates (Figure 4C₃) when the HME content increases from 0% to 50%. For the cells with 10%–35% HME, the magnified images suggest that the needle-like precipitation is

tiny in length and thin in diameter, and their amount rises when the HME content increases (Figure S38). For the cells with 50% HME, the moss-like Li₂S seems to tightly stick on the CP electrode, and their thickness is much thinner compared with that of the chunk-like precipitates in the cells without HME. In brief, the above experimental results at the cell level illustrate that the deteriorated LiPS cathodic kinetics in weakly solvating electrolytes alters the Li₂S precipitation morphology, restricts the Li₂S precipitation extent, and limits the LiPS cathodic performances.

Based on the above theoretical and experimental evaluations, the intrinsic LiPS kinetics are severely impaired as the electrolyte solvating power is weakened, and the sharply increased η_{act} is blamed as the key kinetic limitation. Considering the electrocatalysis strategies are widely adopted to accelerate the intrinsic LiPS kinetics,⁵³ TiN nanoparticles serving as LiPS electrocatalysts are employed into Li–S batteries with high-HME-content electrolytes to boost the LiPS redox kinetics (Figure S39 and S40).

To examine the effect of TiN electrocatalysts in reducing η_{act} , GITT measurements were conducted in Li–S full cells with the TiN electrocatalyst and HME electrolyte (taking 35% HME electrolyte as an example, Figure 5A). The equilibrium potentials for both the charge and the discharge processes are not altered when comparing the cells with and without TiN (*e.g.*, the second discharge plateau voltages in both systems are 2.18 V), manifesting that the introduction of electrocatalysts does not change the thermodynamics of LiPS conversion. On the contrary, the working voltages and the overall polarizations are significantly optimized in the system with electrocatalysts. Specifically, taking the discharge process as an example, the

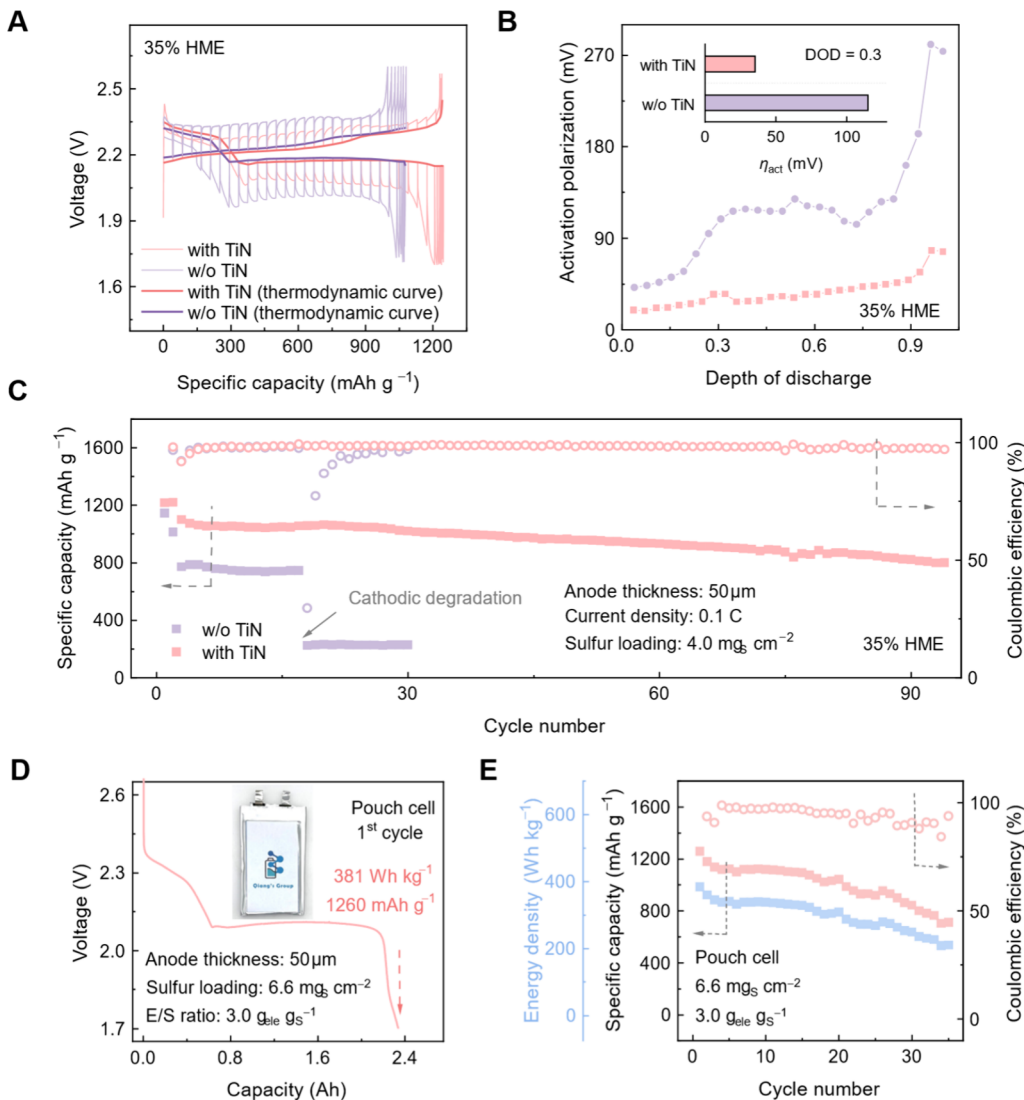


Figure 5. Reducing the activation polarization in weakly solvating electrolytes by introducing TiN electrocatalysts. (A) GITT profiles of Li–S full cells adopting HME electrolytes with or without TiN electrocatalysts. (B) Profiles of activation polarization versus DOD and their comparison at DOD = 0.3 (the inset figure). (C) Long-term cycling performances of Li–S coin cells. (D) 1st cycle and (E) cycling performances of 400 Wh kg^{-1} -level 2.5 Ah pouch cells with HME electrolyte and TiN electrocatalyst (inset: optical photograph of the pouch cell). Note that the energy density is calculated based on the total mass of the pouch cell.

values of η_{act} are greatly reduced (e.g., from 115 to 35.2 mV at the DOD = 0.3) and their proportions in the total polarization prominently decrease, suggesting the intrinsic interfacial charge transfer kinetics is superiorly enhanced (Figure 5B and Figure S41). Additionally, compared with the alteration in η_{act} , the values of η_{con} in the cells with or without electrocatalysts are not changed much (Figure S42). The above results in working Li–S full cells evidently verify our original intention of introducing electrocatalysts to accelerate the intrinsic LiPS charge transfer kinetics, and the η_{act} is indeed reduced in weakly solvating electrolytes by using electrocatalysts. The TiN electrocatalyst is also adopted in the TTE-based Li–S full cells, and the η_{act} can also be significantly reduced (Figure S43). The analogous results in the HME and TTE systems evidently manifest the universality of adopting electrocatalysis strategies to accelerate the LiPS charge transfer kinetics and reduce the values of η_{act} .

Worthy to be noted, the original purpose to introduce weakly solvating electrolytes is to mitigate the anodic issues

and promise practical Li–S batteries with stable cycling performances. Thus, when the unbearable cathodic polarizations for Li–S batteries with weakly solvating electrolytes are eliminated, high cathodic and anodic performances should be concurrently achieved. In this way, Li–S batteries coupled with the TiN electrocatalyst and HME electrolyte were assembled with limited anode excess (using ultrathin lithium metal anodes that are 50 μm in thickness, Figure 5C). As expected, the Li–S cells with the TiN electrocatalyst exhibit an ultrahigh specific capacity over 1200 mAh g^{-1} and stably operate for nearly 100 cycles, while the Li–S cells without the TiN electrocatalyst can only operate for 17 cycles due to cathodic degradation. In detail, for the Li–S cells without the TiN electrocatalyst, the continuously increasing cathodic polarization renders the discharge voltage reaching the cutoff voltage in advance, which induces the sudden capacity loss during cycling (Figure S44). On the contrary, the charge–discharge profiles remain stable in the Li–S cells with the TiN electrocatalyst and HME electrolyte even after 95 cycles

(Figure S45). Notably, the cells with TiN but without HME can only operate stably for no more than 60 cycles due to anodic failure, illustrating that the success of long-term cycling can only be achieved when both the anodic and cathodic performances are rationally regulated (Figure S46).

To fully demonstrate the feasibility of employing TiN electrocatalysts and HME electrolyte in practical Li–S batteries, 2.5 Ah-level pouch cells were assembled with 50 μm -thick lithium anodes and 6.6 mg s cm^{-2} -loading sulfur cathodes (Figures S47 and S48). In detail, the electrolyte/sulfur (E/S) ratio was set to be as low as 3.0 $\text{g}_{\text{ele}} \text{g}_\text{s}^{-1}$ to achieve high energy density based on the actual mass of the pouch cells with all the components included (Figure S49). Under practical working conditions, the pouch cells with the TiN electrocatalyst and HME electrolyte exhibit superior performances regarding an ultrahigh energy density of 381 Wh kg^{-1} and an excellent specific capacity of 1260 mAh g^{-1} (Figure S5D). Moreover, the pouch cell stably operates for 35 cycles with an average CE around 95%, manifesting the concurrent achievement of high cathodic and anodic performances (Figure S5E). The success of concurrently using TiN electrocatalysts and HME electrolyte regarding high energy density and stable cycling lifespan in practical Li–S pouch cells evidently illustrates the high promise of using weakly solvating electrolytes in constructing high-energy-density and long-cycling Li–S batteries when the cathodic kinetics can be fully guaranteed.

CONCLUSIONS

The cathodic LiPS kinetics in weakly solvating electrolyte is systematically investigated to reveal the kinetic degradation mechanism as the electrolyte solvating power gets weakened. Polarization decoupling analysis identifies that the activation polarization instead of concentration or ohmic polarization dramatically increases as the dominant kinetic limitation, as the electrolyte solvating power is weakened. Further mechanism investigation indicates that the enlarged activation polarization originates from the raised charge-transfer activation energy and changed rate-determining step. To address the above kinetic issue, TiN is introduced as an effective LiPS electrocatalyst to overcome unbearable activation polarization. Consequently, Li–S batteries with weakly solvating HME electrolyte and TiN electrocatalysts exhibit reduced polarizations, higher specific capacity, prolonged cycling lifetime, and an actual energy density of 381 Wh kg^{-1} in 2.5 Ah-level pouch cells. This work not only elucidates the cathodic LiPS kinetic mechanism and emphasizes electrocatalytic regulation in protective weakly solvating electrolytes but also inspires further comprehension on designing high-energy-density and long-cycling Li–S batteries.

ASSOCIATED CONTENT

Supporting Information

The Supporting Information is available free of charge at <https://pubs.acs.org/doi/10.1021/jacs.4c02603>.

Complete experimental details, additional material characterization, and electrochemical performance (PDF)

AUTHOR INFORMATION

Corresponding Authors

Bo-Quan Li – Advanced Research Institute of Multidisciplinary Science and School of Materials Science and Engineering, Beijing Institute of Technology, Beijing 100081, China;  orcid.org/0000-0002-9544-5795; Email: libq@bit.edu.cn

Qiang Zhang – Beijing Key Laboratory of Green Chemical Reaction Engineering and Technology, Department of Chemical Engineering, Tsinghua University, Beijing 100084, China;  orcid.org/0000-0002-3929-1541; Email: zhang-qiang@mails.tsinghua.edu.cn

Authors

Xi-Yao Li – Beijing Key Laboratory of Green Chemical Reaction Engineering and Technology, Department of Chemical Engineering, Tsinghua University, Beijing 100084, China;  orcid.org/0000-0003-2366-8591

Shuai Feng – College of Chemistry and Chemical Engineering, Taishan University, Tai'an, Shandong 271021, China;  orcid.org/0000-0002-8604-2097

Yun-Wei Song – Beijing Key Laboratory of Green Chemical Reaction Engineering and Technology, Department of Chemical Engineering, Tsinghua University, Beijing 100084, China

Chang-Xin Zhao – Beijing Key Laboratory of Green Chemical Reaction Engineering and Technology, Department of Chemical Engineering, Tsinghua University, Beijing 100084, China;  orcid.org/0000-0003-3133-0814

Zheng Li – Beijing Key Laboratory of Green Chemical Reaction Engineering and Technology, Department of Chemical Engineering, Tsinghua University, Beijing 100084, China

Zi-Xian Chen – Advanced Research Institute of Multidisciplinary Science and School of Materials Science and Engineering, Beijing Institute of Technology, Beijing 100081, China;  orcid.org/0000-0002-9121-6506

Qian Cheng – Advanced Research Institute of Multidisciplinary Science and School of Materials Science and Engineering, Beijing Institute of Technology, Beijing 100081, China

Xiang Chen – Beijing Key Laboratory of Green Chemical Reaction Engineering and Technology, Department of Chemical Engineering, Tsinghua University, Beijing 100084, China;  orcid.org/0000-0002-7686-6308

Xue-Qiang Zhang – Advanced Research Institute of Multidisciplinary Science and School of Materials Science and Engineering, Beijing Institute of Technology, Beijing 100081, China;  orcid.org/0000-0003-2856-1881

Jia-Qi Huang – Advanced Research Institute of Multidisciplinary Science and School of Materials Science and Engineering, Beijing Institute of Technology, Beijing 100081, China;  orcid.org/0000-0001-7394-9186

Complete contact information is available at:

<https://pubs.acs.org/10.1021/jacs.4c02603>

Author Contributions

All authors have given approval to the final version of the manuscript.

Notes

The authors declare no competing financial interest.

ACKNOWLEDGMENTS

This work was supported by National Key Research and Development Program (2021YFB2400300, 2021YFB2500300), National Natural Science Foundation of China (22109007, 22109086, 22209010), and the Tsinghua University Initiative Scientific Research Program. The authors acknowledged the support from Tsinghua National Laboratory for Information Science and Technology for theoretical simulations. We thank Shu-Yu Sun, Jia-Ning Liu, Liang Shen, and Dr. Meng Zhao for the helpful discussion.

REFERENCES

- (1) Hassan, Y.; Park, J. H.; Crawford, M. L.; Sadhanala, A.; Lee, J.; Sadighian, J. C.; Mosconi, E.; Shivanna, R.; Radicchi, E.; Jeong, M.; et al. Ligand-engineered bandgap stability in mixed-halide perovskite LEDs. *Nature* **2021**, *591* (7848), 72–77.
- (2) Cheng, X.-B.; Zhang, R.; Zhao, C.-Z.; Zhang, Q. Toward safe lithium metal anode in rechargeable batteries: A review. *Chem. Rev.* **2017**, *117* (15), 10403–10473.
- (3) Liu, Y.; Tao, X.; Wang, Y.; Jiang, C.; Ma, C.; Sheng, O.; Lu, G.; Lou, X. W. Self-assembled monolayers direct a LiF-rich interphase toward long-life lithium metal batteries. *Science* **2022**, *375* (6582), 739–745.
- (4) Harper, G.; Sommerville, R.; Kendrick, E.; Driscoll, L.; Slater, P.; Stolkin, R.; Walton, A.; Christensen, P.; Heidrich, O.; Lambert, S.; et al. Recycling lithium-ion batteries from electric vehicles. *Nature* **2019**, *575* (7781), 75–86.
- (5) Yao, N.; Chen, X.; Fu, Z.-H.; Zhang, Q. Applying classical, ab Initio, and machine-learning molecular dynamics simulations to the liquid electrolyte for rechargeable batteries. *Chem. Rev.* **2022**, *122* (12), 10970–11021.
- (6) Zhang, Q. Fluorinated interphases. *Nat. Nanotechnol.* **2018**, *13* (8), 623–624.
- (7) Cha, E.; Patel, M. D.; Park, J.; Hwang, J.; Prasad, V.; Cho, K.; Choi, W. 2D MoS₂ as an efficient protective layer for lithium metal anodes in high-performance Li–S batteries. *Nat. Nanotechnol.* **2018**, *13* (4), 337–344.
- (8) Li, X.-Y.; Feng, S.; Zhao, M.; Zhao, C.-X.; Chen, X.; Li, B.-Q.; Huang, J.-Q.; Zhang, Q. Surface Gelation on Disulfide Electrocatalysts in Lithium–Sulfur Batteries. *Angew. Chem.* **2022**, *61* (7), No. e202114671.
- (9) Li, Z.; Sami, I.; Yang, J.; Li, J.; Kumar, R. V.; Chhowalla, M. Lithiated metallic molybdenum disulfide nanosheets for high-performance lithium–sulfur batteries. *Nat. Energy* **2023**, *8* (1), 84–93.
- (10) Ji, X.; Lee, K. T.; Nazar, L. F. A highly ordered nanostructured carbon–sulphur cathode for lithium–sulphur batteries. *Nat. Mater.* **2009**, *8* (6), 500–506.
- (11) Peng, H.-J.; Huang, J.-Q.; Zhang, Q. A review of flexible lithium–sulfur and analogous alkali metal–chalcogen rechargeable batteries. *Chem. Soc. Rev.* **2017**, *46* (17), 5237–5288.
- (12) Zhao, M.; Li, X.-Y.; Chen, X.; Li, B.-Q.; Kaskel, S.; Zhang, Q.; Huang, J.-Q. Promoting the sulfur redox kinetics by mixed organodiselenides in high-energy-density lithium–sulfur batteries. *eScience* **2021**, *1* (1), 44–52.
- (13) Zhao, C.-X.; Li, X.-Y.; Zhao, M.; Chen, Z.-X.; Song, Y.-W.; Chen, W.-J.; Liu, J.-N.; Wang, B.; Zhang, X.-Q.; Chen, C.-M.; et al. Semi-immobilized molecular electrocatalysts for high-performance lithium–sulfur batteries. *J. Am. Chem. Soc.* **2021**, *143* (47), 19865–19872.
- (14) Pan, H.; Chen, J.; Cao, R.; Murugesan, V.; Rajput, N. N.; Han, K. S.; Persson, K.; Estevez, L.; Engelhard, M. H.; Zhang, J.-G.; et al. Non-encapsulation approach for high-performance Li–S batteries through controlled nucleation and growth. *Nat. Energy* **2017**, *2* (10), 813–820.
- (15) Zhao, C.; Xu, G.-L.; Yu, Z.; Zhang, L.; Hwang, I.; Mo, Y.-X.; Ren, Y.; Cheng, L.; Sun, C.-J.; Ren, Y.; et al. A high-energy and long-cycling lithium–sulfur pouch cell via a macroporous catalytic cathode with double-end binding sites. *Nat. Nanotechnol.* **2021**, *16* (2), 166–173.
- (16) Li, X.-Y.; Feng, S.; Zhao, C.-X.; Cheng, Q.; Chen, Z.-X.; Sun, S.-Y.; Chen, X.; Zhang, X.-Q.; Li, B.-Q.; Huang, J.-Q.; et al. Regulating lithium salt to inhibit surface gelation on an electrocatalyst for high-energy-density lithium–sulfur batteries. *J. Am. Chem. Soc.* **2022**, *144* (32), 14638–14646.
- (17) Cheng, Q.; Xu, W.; Qin, S.; Das, S.; Jin, T.; Li, A.; Li, A. C.; Qie, B.; Yao, P.; Zhai, H.; et al. Full dissolution of the whole lithium sulfide family (Li₂S₈ to Li₂S) in a safe eutectic solvent for rechargeable lithium–sulfur batteries. *Angew. Chem., Int. Ed.* **2019**, *58* (17), 5557–5561.
- (18) Shen, Z.; Jin, X.; Tian, J.; Li, M.; Yuan, Y.; Zhang, S.; Fang, S.; Fan, X.; Xu, W.; Lu, H.; et al. Cation-doped ZnS catalysts for polysulfide conversion in lithium–sulfur batteries. *Nat. Catal.* **2022**, *5* (6), 555–563.
- (19) Fu, Y.; Wu, Z.; Yuan, Y.; Chen, P.; Yu, L.; Yuan, L.; Han, Q.; Lan, Y.; Bai, W.; Kan, E.; Huang, C.; Ouyang, X.; Wang, X.; Zhu, J.; Lu, J.; et al. Switchable encapsulation of polysulfides in the transition between sulfur and lithium sulfide. *Nat. Commun.* **2020**, *11* (1), 845.
- (20) Peng, H.-J.; Huang, J.-Q.; Liu, X.-Y.; Cheng, X.-B.; Xu, W.-T.; Zhao, C.-Z.; Wei, F.; Zhang, Q. Healing high-loading sulfur electrodes with unprecedented long cycling life: spatial heterogeneity control. *J. Am. Chem. Soc.* **2017**, *139* (25), 8458–8466.
- (21) Zak, J. J.; Kim, S. S.; Laskowski, F. A. L.; See, K. A. An exploration of sulfur redox in lithium battery cathodes. *J. Am. Chem. Soc.* **2022**, *144* (23), 10119–10132.
- (22) Zhao, M.; Li, B.-Q.; Zhang, X.-Q.; Huang, J.-Q.; Zhang, Q. A perspective toward practical lithium–sulfur batteries. *ACS Cent. Sci.* **2020**, *6* (7), 1095–1104.
- (23) Zhang, Y.; Heim, F. M.; Song, N.; Bartlett, J. L.; Li, X. New insights into mossy Li induced anode degradation and its formation mechanism in Li–S batteries. *ACS Energy Lett.* **2017**, *2* (12), 2696–2705.
- (24) Gordin, M. L.; Dai, F.; Chen, S.; Xu, T.; Song, J.; Tang, D.; Azimi, N.; Zhang, Z.; Wang, D. Bis(2,2,2-trifluoroethyl) ether as an electrolyte co-solvent for mitigating self-discharge in lithium–sulfur batteries. *ACS Appl. Mater. Interfaces* **2014**, *6* (11), 8006–8010.
- (25) Mikhaylik, Y. V.; Akridge, J. R. Polysulfide shuttle study in the Li/S battery system. *J. Electrochem. Soc.* **2004**, *151* (11), A1969.
- (26) Chen, Z.-X.; Zhao, M.; Hou, L.-P.; Zhang, X.-Q.; Li, B.-Q.; Huang, J.-Q. Toward practical high-energy-density lithium–sulfur pouch cells: a review. *Adv. Mater.* **2022**, *34* (35), No. 2201555.
- (27) Xu, R.; Belharouak, I.; Li, J. C. M.; Zhang, X.; Bloom, I.; Bareño, J. Role of polysulfides in self-healing lithium–sulfur batteries. *Adv. Energy Mater.* **2013**, *3* (7), 833–838.
- (28) Dörfler, S.; Althues, H.; Härtel, P.; Abendroth, T.; Schumm, B.; Kaskel, S. Challenges and key parameters of lithium–sulfur batteries on pouch cell level. *Joule* **2020**, *4* (3), 539–554.
- (29) Li, G.; Wang, S.; Zhang, Y.; Li, M.; Chen, Z.; Lu, J. Revisiting the role of polysulfides in lithium–sulfur batteries. *Adv. Mater.* **2018**, *30* (22), No. 1705590.
- (30) Hua, W.; Shang, T.; Li, H.; Sun, Y.; Guo, Y.; Xia, J.; Geng, C.; Hu, Z.; Peng, L.; Han, Z.; et al. Optimizing the p charge of S in p-block metal sulfides for sulfur reduction electrocatalysis. *Nat. Catal.* **2023**, *6* (2), 174–184.
- (31) Su, C.-C.; He, M.; Amine, R.; Amine, K. A selection rule for hydrofluoroether electrolyte cosolvent: establishing a linear free-energy relationship in lithium–sulfur batteries. *Angew. Chem., Int. Ed.* **2019**, *58* (31), 10591–10595.
- (32) Bieker, G.; Wellmann, J.; Kolek, M.; Jalkanen, K.; Winter, M.; Bieker, P. Influence of cations in lithium and magnesium polysulfide solutions: dependence of the solvent chemistry. *Phys. Chem. Chem. Phys.* **2017**, *19* (18), 11152–11162.
- (33) Liu, T.; Li, H.; Yue, J.; Feng, J.; Mao, M.; Zhu, X.; Hu, Y.-S.; Li, H.; Huang, X.; Chen, L.; et al. Ultralight electrolyte for high-energy lithium–sulfur pouch cells. *Angew. Chem., Int. Ed.* **2021**, *60* (32), 17547–17555.

- (34) Liu, Y.; Elias, Y.; Meng, J.; Aurbach, D.; Zou, R.; Xia, D.; Pang, Q. Electrolyte solutions design for lithium–sulfur batteries. *Joule* 2021, 5 (9), 2323–2364.
- (35) Li, Z.; Zhou, Y.; Wang, Y.; Lu, Y.-C. Solvent-mediated Li_2S electrodeposition: a critical manipulator in lithium–sulfur batteries. *Adv. Energy Mater.* 2019, 9 (1), No. 1802207.
- (36) Gupta, A.; Bhargav, A.; Manthiram, A. Highly solvating electrolytes for lithium–sulfur batteries. *Adv. Energy Mater.* 2019, 9 (6), No. 1803096.
- (37) Cuisinier, M.; Hart, C.; Balasubramanian, M.; Garsuch, A.; Nazar, L. F. Radical or not radical: revisiting lithium–sulfur electrochemistry in nonaqueous electrolytes. *Adv. Energy Mater.* 2015, 5 (16), No. 1401801.
- (38) Zhang, G.; Peng, H.-J.; Zhao, C.-Z.; Chen, X.; Zhao, L.-D.; Li, P.; Huang, J.-Q.; Zhang, Q. The radical pathway based on a lithium-metal-compatible high-dielectric electrolyte for lithium–sulfur batteries. *Angew. Chem., Int. Ed.* 2018, 57 (51), 16732–16736.
- (39) Zhong, N.; Lei, C.; Meng, R.; Li, J.; He, X.; Liang, X. Electrolyte solvation chemistry for the solution of high-donor-number solvent for stable Li–S batteries. *Small* 2022, 18 (16), No. 2200046.
- (40) Cheng, L.; Curtiss, L. A.; Zavadil, K. R.; Gewirth, A. A.; Shao, Y.; Gallagher, K. G. Sparingly solvating electrolytes for high energy density lithium–sulfur batteries. *ACS Energy Lett.* 2016, 1 (3), 503–509.
- (41) Shyamsunder, A.; Beichel, W.; Klose, P.; Pang, Q.; Scherer, H.; Hoffmann, A.; Murphy, G. K.; Krossing, I.; Nazar, L. F. Inhibiting polysulfide shuttle in lithium–sulfur batteries through low-ion-pairing salts and a triflamide solvent. *Angew. Chem., Int. Ed.* 2017, 56 (22), 6192–6197.
- (42) Zhang, X.-Q.; Jin, Q.; Nan, Y.-L.; Hou, L.-P.; Li, B.-Q.; Chen, X.; Jin, Z.-H.; Zhang, X.-T.; Huang, J.-Q.; Zhang, Q. Electrolyte structure of lithium polysulfides with anti-reductive solvent shells for practical lithium–sulfur batteries. *Angew. Chem., Int. Ed.* 2021, 60 (28), 15503–15509.
- (43) Hou, L.-P.; Li, Z.; Yao, N.; Bi, C.-X.; Li, B.-Q.; Chen, X.; Zhang, X.-Q.; Zhang, Q. Weakening the solvating power of solvents to encapsulate lithium polysulfides enables long-cycling lithium–sulfur batteries. *Adv. Mater.* 2022, 34, No. 2205284.
- (44) Cai, G.; Gao, H.; Li, M.; Gupta, V.; Holoubek, J.; Pascal, T. A.; Liu, P.; Chen, Z. Partially ion-paired solvation structure design for lithium–sulfur batteries under extreme operating conditions. *Angew. Chem., Int. Ed.* 2024, 63 (5), No. e202316786.
- (45) Hou, L.-P.; Zhang, X.-Q.; Yao, N.; Chen, X.; Li, B.-Q.; Shi, P.; Jin, C.-B.; Huang, J.-Q.; Zhang, Q. An encapsulating lithium-polysulfide electrolyte for practical lithium–sulfur batteries. *Chem.* 2022, 8 (4), 1083–1098.
- (46) Cai, G.; Holoubek, J.; Li, M.; Gao, H.; Yin, Y.; Yu, S.; Liu, H.; Pascal, T. A.; Liu, P.; Chen, Z. Solvent selection criteria for temperature-resilient lithium–sulfur batteries. *Proc. Natl. Acad. Sci.* 2022, 119 (28), No. e2200392119.
- (47) Sun, K.; Wu, Q.; Tong, X.; Gan, H. Electrolyte with low polysulfide solubility for Li–S batteries. *ACS Appl. Energy Mater.* 2018, 1 (6), 2608–2618.
- (48) See, K. A.; Wu, H.-L.; Lau, K. C.; Shin, M.; Cheng, L.; Balasubramanian, M.; Gallagher, K. G.; Curtiss, L. A.; Gewirth, A. A. Effect of hydrofluoroether cosolvent addition on Li solvation in acetonitrile-based solvate electrolytes and its influence on S reduction in a Li–S battery. *ACS Appl. Mater. Interfaces* 2016, 8 (50), 34360–34371.
- (49) Kong, L.; Yin, L.; Xu, F.; Bian, J.; Yuan, H.; Lu, Z.; Zhao, Y. Electrolyte solvation chemistry for lithium–sulfur batteries with electrolyte-lean conditions. *J. Energy Chem.* 2021, 55, 80–91.
- (50) Gao, X.; Yu, Z.; Wang, J.; Zheng, X.; Ye, Y.; Gong, H.; Xiao, X.; Yang, Y.; Chen, Y.; Bone, S. E.; et al. Electrolytes with moderate lithium polysulfide solubility for high-performance long-calendar-life lithium–sulfur batteries. *Proc. Natl. Acad. Sci.* 2023, 120 (31), No. e2301260120.
- (51) Peng, L.; Wei, Z.; Wan, C.; Li, J.; Chen, Z.; Zhu, D.; Baumann, D.; Liu, H.; Allen, C. S.; Xu, X.; et al. A fundamental look at electrocatalytic sulfur reduction reaction. *Nat. Catal.* 2020, 3 (9), 762–770.
- (52) Feng, S.; Fu, Z.-H.; Chen, X.; Li, B.-Q.; Peng, H.-J.; Yao, N.; Shen, X.; Yu, L.; Gao, Y.-C.; Zhang, R.; et al. An electrocatalytic model of the sulfur reduction reaction in lithium–sulfur batteries. *Angew. Chem.* 2022, 61 (52), No. e202211448.
- (53) Zhong, Y.; Wang, Q.; Bak, S.-M.; Hwang, S.; Du, Y.; Wang, H. Identification and catalysis of the potential-limiting step in lithium–sulfur batteries. *J. Am. Chem. Soc.* 2023, 145 (13), 7390–7396.